Neutron scattering study of two-magnon states in the quantum magnet copper nitrate

D. A. Tennant,[1,2,3,4] C. Broholm,[5,6] D. H. Reich,[7] S. E. Nagler,[3] G. E. Granroth,[3] T. Barnes,[7,8] K. Damle,[9] G. Xu,[5] Y. Chen,[5] and B. C. Sales[3]

[1]*ISIS Facility, Rutherford Appleton Laboratory, Didcot OX11 0QX, Oxon., United Kingdom*
[2]*Oxford Physics, Clarendon Laboratory, Parks Road, Oxford OX1 3PU, United Kingdom*
[3]*Solid State Division, Oak Ridge National Laboratory, Oak Ridge, Tennessee 37831-6393*
[4]*Department of Physics and Chemistry, Risø National Laboratory, Roskilde, DK-4000, Denmark*
[5]*Department of Physics and Astronomy, The Johns Hopkins University, Baltimore, Maryland 21218*
[6]*NIST Center for Neutron Research, National Institute of Standards and Technology, Gaithersburg, Maryland 20899*
[7]*Department of Physics and Astronomy, University of Tennessee, Knoxville, Tennessee 37996-1501*
[8]*Physics Division, Oak Ridge National Laboratory, Oak Ridge, Tennessee 37831-6373*
[9]*Physics Department, Harvard University, Cambridge, Massachusetts 02138*

(Received 29 July 2002; revised manuscript received 30 September 2002; published 27 February 2003)

We report measurements of the two-magnon states in a dimerized antiferromagnetic chain material, copper nitrate $[Cu(NO_3)_2 \cdot 2.5D_2O]$. Using inelastic neutron scattering we have measured the one- and two-magnon excitation spectra in a large single crystal. The data are in excellent agreement with a perturbative expansion of the alternating Heisenberg Hamiltonian from the strongly dimerized limit. The expansion predicts a two-magnon bound state for $q \sim (2n+1)\pi d$ which is consistent with the neutron scattering data.

DOI: 10.1103/PhysRevB.67.054414 PACS number(s): 75.10.Jm, 75.40.Gb, 78.70.Nx

I. INTRODUCTION

The basic physics of the elementary one-magnon excitations of lower-dimensional quantum antiferromagnets can now be regarded as well established, both theoretically and experimentally, through studies of materials that are reasonably accurate realizations of the spin Hamiltonians. In contrast, higher excitations such as multimagnon continua and bound states have attracted relatively little attention. This topic may prove to be a fascinating area for the application of few- and many-body techniques, and will involve interesting and nontrivial results in band structure, band mixing, bound-state formation, phase transitions through the formation of condensates of magnetic excitations,[1–7] and other collective phenomena.

Although some aspects of the physics of low-lying multimagnon states can be inferred from model Hamiltonians using standard theoretical techniques, few experimental studies of these higher excitations have been reported to date. Experimental difficulties that have precluded such work include relatively weak couplings of probes to these higher excitations, dominant contributions from the lowest one-magnon excitations, and resolution requirements in energy and wave number that are beyond the capabilities of most techniques.

High-resolution inelastic neutron scattering should prove to be an ideal technique for observing some of these higher magnetic excitations. One can control both energy and momentum transfer, so that the existence and spectral weight of higher magnetic excitations can be established and quantified. The new generation of high-intensity neutron sources combined with high-resolution detectors should allow the observation of details of the multimagnon excitation spectrum such as band boundaries, quantitative determination of the dynamical correlation function $\mathcal{S}(\mathbf{Q},\omega)$ and discontinuities within a band,[8] and weakly bound states just below the band edge. The principle limitation in this approach may be the unavoidable $\Delta S = 1$ selection rule of magnetic neutron scattering, so that one can only reach spin $S=1$ excitations given an $S=0$ ground state and an isotropic spin Hamiltonian. Other techniques such as Raman scattering can be used to study certain of these higher excitations, *albeit* with strong constraints on the accessible spin and momentum quantum numbers.

Systems that appear especially interesting for studies of higher magnetic excitations at present are quasi-one-dimensional (quasi-1D) spin chains and spin ladders, since many of these have gaps and hence will have separated bands of higher excitations and perhaps bound states of magnons. The alternating Heisenberg antiferromagnetic chain (AHC) with spin 1/2 is an example of such a system; with any amount of alternation $0<\alpha<1$ (where $\alpha \equiv J2/J1$) the AHC has an energy gap in its one-magnon dispersion with a second gap to the multimagnon continuum (see Fig. 1), and two-magnon bound states with spin 0 and spin 1 are predicted.[9] The AHC is also attractive because of its relative simplicity and because of recent extensive theoretical studies of the low-energy excitations in this model.

In this paper we present results from an inelastic neutron scattering study of higher magnetic excitations in copper nitrate $[Cu(NO_3)_2 \cdot 2.5D_2O]$, which was recently confirmed by neutron scattering[10] to be an accurate realization of a strongly alternating Heisenberg antiferromagnetic chain. This material is especially attractive because the alternation parameter $\alpha \approx 0.27$ is close to the value predicted to maximize the separation of the spin-1 two-magnon bound state from the continuum.[11] In addition it is relatively easy to prepare large single crystals of this material, which compensates for the weak neutron scattering intensity from the higher magnetic excitations.

The paper is arranged as follows: Section II summarizes important results from the theory of the ground and excited states of the alternating Heisenberg chain. Section III re-

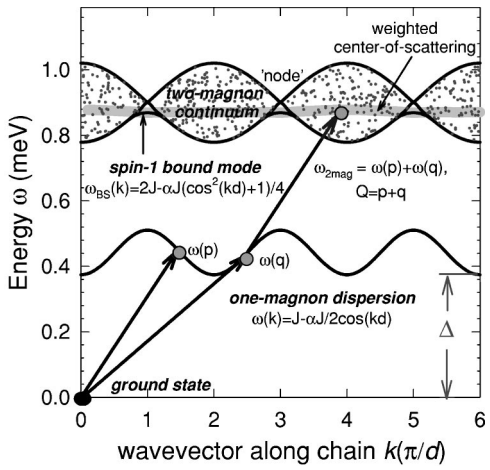

FIG. 1. The $S=1$ excitation spectrum of the spin-1/2 alternating Heisenberg chain with moderately strong dimerization. The parameters used are $J=0.45$ meV and $\alpha=0.27$ (as fit to copper nitrate neutron scattering data.) There is an energy gap Δ from the $S=0$ ground state to the $S=1$ triplet magnon band. The two-magnon continuum states are also shown; these have energies and wave vectors given by the sum of two independent one-magnon excitations. A $S=1$ bound state is predicted to lie just below the two-magnon continuum for small wave vectors near $k=\pi/d$, where the continuum has minimum width.

views the magnetic properties of $Cu(NO_3)_2\cdot 2.5D_2O$, or CN for short. Section IV presents the results of our measurements, with the analysis in terms of the model given in Sec. V. A discussion of the results is given in Sec. VI, with conclusions in Sec. VII. Additional theoretical results for two-magnon excitations in this model are given in the Appendix.

II. THEORY

The spin-1/2 alternating Heisenberg chain has received much attention in the theoretical literature. This simple model plays a central role in the study of the spin-Peierls effect and is also known to provide an accurate description of the magnetic properties of many real materials. The model consists of antiferromagnetically coupled Heisenberg spin pairs, ''dimers,'' which are themselves coupled by weaker antiferromagnetic Heisenberg interactions in an alternating chain, as shown in Fig. 2. The Hamiltonian for this model is given by

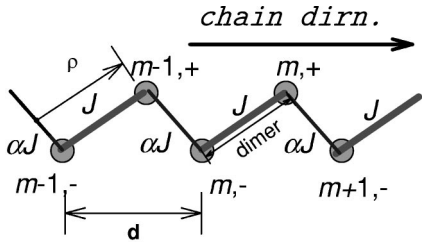

FIG. 2. Alternating chain layout showing dimers coupled together. Each dimer is labeled by an index m, $\boldsymbol{\rho}$ is the separation between dimer spins, and $\mathbf{d}$ is the chain repeat vector.

$$H=\sum_{m=1}^{N/2} J\{\mathbf{S}_{m,-}\cdot\mathbf{S}_{m,+}+\alpha\mathbf{S}_{m,+}\cdot\mathbf{S}_{m+1,-}\}, \tag{1}$$

where N is the number of spins in the chain, $J>0$ (also called J_1) is the intradimer coupling, αJ (also J_2) is the interdimer coupling, and α is allowed the range $0<\alpha<1$. The index m labels the dimers, and $-$ and $+$ denote left and right spins. The position of each spin is given by $\mathbf{r}_{m,\pm}=m\mathbf{d}\pm\boldsymbol{\rho}/2$, where $\mathbf{d}$ is the chain repeat vector, and $\boldsymbol{\rho}$ is the intradimer separation.

This model has a nontrivial spin-0 ground state, and for all α in the allowed range $0<\alpha<1$ has a gap to the first excitation, which is a band of spin-1 excitations (magnons). In the ''strong-coupling limit'' $\alpha\ll 1$ the ground state approaches a system of uncoupled spin-0 dimers, and the one-magnon excitations can be accurately described as a single dimer excited to spin 1 (an ''exciton''), delocalized on the chain to give states of definite along-chain wave number k. The energies and some matrix elements of these states have been evaluated as power series in the intradimer coupling α.[11,12]

To interpret experimental results approximate analytic forms of the wave functions and energies are useful, and we include calculations of wave functions expanded around the single dimer eigenstates in the Appendix. The one-magnon $S=1$ triplet has a gap energy $\Delta=J-\alpha J/2$ and dispersion to $\mathcal{O}(\alpha)$:

$$\omega_{1\mathrm{mag}}(k)=J-\alpha J/2\cos(kd). \tag{2}$$

This magnon wave function can be visualized as a localized wave packet of magnetic polarization (excitons) along x, y, or z carrying total spin 1 traveling through a featureless singlet background with the gap energy coming from the effort expended in breaking a dimer bond.

Approximate wave functions for the two-magnon states are given in the Appendix. At large separations the magnons do not overlap and they behave as free particles; however, when close they interfere and scatter off each other. In a one-dimensional geometry such scattering conserves particle number, energy, and momentum up to a lattice wave vector, and the scattering introduces a momentum-dependent phase shift in the scattered wave function. The energy of these states [to order $\mathcal{O}(1/N)$] is given by $\omega_{k_1,k_2}(k)=\omega_{1\mathrm{mag}}(k_1)+\omega_{1\mathrm{mag}}(k_2)$, where $k=k_1+k_2$ is the total wave vector. The resulting continuum using Eq. (2) is illustrated in Fig. 1.[8]

As well as elastic scattering of magnons, bound states also form. To appreciate their physical origin consider two dimers, both in excited states, coupled by a single interdimer coupling αJ. In the absence of coupling all the double excited states $S=0$, 1, and 2 have the same energy $2J$. However, the interdimer coupling splits these states. There is an $S=2$ quintuplet of energy $2J+\alpha J/4$ (this energy is higher because the interdimer coupling favors antiferromagnetism whereas the $S=2$ states have all spins along the same direction—ferromagnetic). There is also an $S=1$ triplet of energy $2J-\alpha J/4$; this lowering of energy is purely quantum mechanical and comes from resonance between the two excited dimers. Finally there is an $S=0$ singlet of even lower

TABLE I. Crystallographic data for $Cu(NO_3)_2 \cdot 2.5H_2O$ from Ref. 15 The room-temperature lattice parameters are $a=16.453$, $b=4.936$, $c=15.963$ Å, and $\beta=93.765°$. The Cu ions are at the $8f$ positions at (x,y,z) where $x=0.12613$, $y=0.01352$, and $z=0.11376$. The equivalent positions in the unit cell are given.

Atom	x position	y position	z position
1	x	y	z
2	$1-x$	$1-y$	$1-z$
3	$1-x$	y	$\frac{1}{2}-z$
4	x	$1-y$	$\frac{1}{2}+z$
5	$\frac{1}{2}+x$	$\frac{1}{2}-y$	z
6	$\frac{1}{2}-x$	$\frac{1}{2}+y$	$1-z$
7	$\frac{1}{2}-x$	$\frac{1}{2}-y$	$\frac{1}{2}-z$
8	$\frac{1}{2}+x$	$\frac{1}{2}+y$	$\frac{1}{2}+z$

energy, $2J-\alpha J/2$, which gains resonance and also antiferromagnetic energy due to the spins in neighboring dimers pointing in opposite directions.

As the $S=0$ and 1 states with excited dimers neighboring each other have lower energy than two well-separated excited dimers (by $\alpha J/4$ and $\alpha J/2$, respectively) there is a short-range attractive potential. Magnons can be confined within the potential well (bound states) as long as the relative kinetic energy between the magnons is smaller than the interaction energy.

This situation applies to the bound states in the AHC: the $S=0$ mode at all wave vectors and the $S=1$ mode over limited wave vectors around the node points. These are positions where the kinetic energy is small compared to the binding potential. The $S=1$ bound state is visible to neutron scattering and has a dispersion[9,13]

$$\omega_{\mathrm{BS}}=2J-\frac{\alpha J}{4}[4\cos^2(kd/2)+1].$$

The bound state is characterized by a probability amplitude for the separation between the two magnons that drops exponentially with distance (see the Appendix for more details). These $S=1$ bound states exist only over the range $|n\pi-kd|\leqslant\pi/3$, where n is an odd integer; see Fig. 1.

III. MAGNETIC PROPERTIES OF $Cu(NO_3)_2 \cdot 2.5D_2O$

The structural and magnetic properties of CN have been thoroughly investigated and shown to be near ideal. The structure of $Cu(NO_3)_2 \cdot 2.5H_2O$ was investigated by Garaj[14] and Morosin,[15] and was shown to have a monoclinic crystal structure with space group $I12/c1$ (Ref. 16) and the lattice parameters and crystallographic copper positions given in Table I. The deuterated form $Cu(NO_3)_2 \cdot 2.5D_2O$ we studied has low-temperature ($T=3$ K) lattice parameters $a=16.1$, $b=4.9$, $c=15.8$ Å, and $\beta=92.9°$.[10]

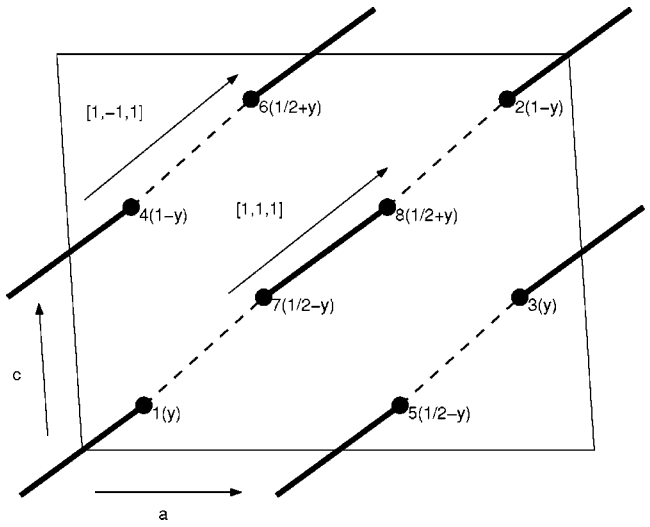

FIG. 3. Positions of copper ions projected onto the *ac* plane for $Cu(NO_3)_2 \cdot 2.5D_2O$. The atom positions are those detailed in Table I. Two sets of identical chains run in the [1,1,1] and [1,1,1] directions, respectively.

The magnetism of CN arises from the Cu^{2+} ions. Crystal electric fields from the oxygen ligands surrounding the Cu^{2+} ions quench their orbital moments, leaving a near-isotropic spin-1/2 moment with g values that show a small easy-axis anisotropy along the crystallographic b direction; the values are $g_{\|\mathbf{b}}=2.33$ and $g_{\perp\mathbf{b}}=2.09$.[17] Magnetic superexchange in this material is mediated by long double Cu-O-O-Cu exchange paths, which accounts for the rather weak exchange interaction observed in CN.

The exchange couplings of CN were studied by Eckert *et al.* in Ref. 18 and are illustrated in Fig. 3. The dominant magnetic exchange integral J is between pairs of spins (copper positions 7 and 8 and equivalent pairs; cf. Fig. 3) forming dimers with a separation of 5.3 Å. These dimers separated by *crystal vector* $\mathbf{u}=[u_1,u_2,u_3]\equiv u_1\mathbf{a}+u_2\mathbf{b}+u_3\mathbf{c}$ are coupled together by exchanges $J'_{\mathbf{u}}$; the only exchange paths of appreciable strength are $J'_{[1/2,\pm1/2,1/2]}$, connected via bonds between 1 and 7 and equivalent (bond length 6.2 Å). This results in two sets of $S=1/2$ alternating Heisenberg chains running in the [1,1,1] and [1,1,1] directions of the crystal with repetition every $\mathbf{d}=[1,1,1]/2$ and $\mathbf{d}'=[1,1,1]/2$, respectively (repeat distance $d=11.3$ Å); the corresponding intradimer vectors are $\boldsymbol{\rho}=[0.252,\pm0.027,0.228]$ (where the x,y,z positions from Table I have been used). Inelastic neutron scattering measurements[10] have recently further confirmed the model alternating Heisenberg chain properties of CN and have shown that the dominant collective excitations are indeed the gapped triplet of magnons expected for the AHC.

Approximate ground-state energy

Bulk magnetic measurements give information on the gap, exchange, and ground-state energies of the spin chains

in copper nitrate. Measurements of the effect of applied magnetic field show that spin-flop (SF) ordering is induced in CN above a critical field $B_{c1} \approx 2.7$ T, with a transition to full alignment at $B_{c2} \approx 4.3$ T, and there are no demagnetization effects in the zero-temperature limit.[19] As the orbital moment on the Cu^{2+} ions is quenched by the crystal electric field and demagnetization effects are negligible, the field B_{c1} can be used to directly give the excitation gap energy to the one-magnon states, and Diederix *et al.* report a value of $\Delta = 0.378 \pm .007$ meV.[19]

The gap can be inferred from the transition field because the magnons carry spin quantum numbers $S^z = 1,0,-1$ and are split into three dispersive modes shifted by a Zeeman energy with respect to each other. The ground state by virtue of its spin-0 quantum number is unaffected by the field, and the transition occurs when the Zeeman energy of the lowest mode closes the gap and magnons condense into the ground state. The long-range order itself is due to weak couplings between the chains.

The high-field transition B_{c2} yields further important information. It is where all the low-lying magnons are completely condensed into the ground state and the spins are fully aligned along the field. The fully aligned state is an exact eigenstate, and for an unfrustrated quantum magnet the transition field gives the sum of exchange couplings $g\mu_B B_{c2} = J + \Sigma_{\mathbf{u}} J'_{\mathbf{u}} = 0.580 \pm 0.007$ meV in the system.[7] An estimate of the ground-state energy of CN can be made using these numbers.

Using the low-temperature isothermal magnetization $M(B) = g\mu_B \langle S^z \rangle_B$ as a measure of the work required to saturate the spin chains from the zero-field quantum ground state, an energy per spin can be inferred. The zero-field ground-state energy per spin e_0 can be estimated via the formula $e_0 \approx e_f - g\mu_B S B_{c2} + \int_0^{B_{c2}} M(B) dB$ where the fully aligned energy per spin is $e_f = (S^2/2)(J + \Sigma_{\mathbf{u}} J'_{\mathbf{u}}) = g\mu_B B_{c2}/8 = 0.0725 \pm 0.001$ meV for a $S = 1/2$ unfrustrated system. Utilizing the 270 mK data of Diederix in Fig. 3 of Ref. 19 (measured using proton resonance) to determine the integral over magnetization gives an experimental ground-state energy per spin $e_0 = -0.174 \pm 0.004$ meV. This is essentially the $T = 0$ result, as the gap activation energy corresponds to 4.4 K.

To estimate thermodynamic properties we approximate the sum of the *interdimer* exchanges by the single coupling $\alpha J = \Sigma_{\mathbf{u}} J'_{\mathbf{u}}$ of Eq. (1). Using the $\mathcal{O}(\alpha^9)$ expansions[11] for $\Delta(\alpha)$ and e_0 gives $J = 0.455 \pm 0.002$ meV and $\alpha = 0.277 \pm 0.006$, in agreement with the results of Refs. 19 and 20, $J = 0.45$ meV and $\alpha = 0.27$. Our calculated values of the thermodynamic parameters $J + \Sigma_{\mathbf{u}} J'_{\mathbf{u}} = 0.581$ meV, $\Delta = 0.379$ meV, and $e_0 = -0.172$ meV agree within error with the experimental values.

IV. EXPERIMENTAL METHOD

A. Neutron scattering

The inelastic neutron scattering cross section[21]

$$\frac{d^2\sigma}{d\Omega d\omega} \propto N \sigma_{mag} \sum_{\alpha,\beta} \frac{k_f}{k_i} |F(\mathbf{Q})|^2 (\delta_{\alpha\beta} - Q_\alpha Q_\beta) \mathcal{S}^{\alpha\beta}(\mathbf{Q},\omega)$$

is proportional to the dynamical response $\mathcal{S}^{\alpha\beta}(\mathbf{Q},\omega)$, where $\mathbf{Q}$ is the wave vector transfer, $F(\mathbf{Q})$ is the magnetic form factor, N is the number of scattering centers, the constant $\sigma_{mag} = 0.2896$ b, k_i and k_f are the momenta of initial and final neutron states, respectively, g is the Landé g factor, and $\alpha = x,y,z$ are Cartesian coordinates. The dynamical response is the space and time Fourier transform of the spin-spin correlation function

$$\mathcal{S}^{\alpha\beta}(\mathbf{Q},\omega) = \frac{1}{2\pi N} \sum_{i,j} \int \exp\{i[\omega t + \mathbf{Q}\cdot(\mathbf{r}_i - \mathbf{r}_j]\} \times \langle S_i^\alpha(0) S_j^\beta(t) \rangle dt,$$

where i and j labels sites of the system. For the AHC, Eq. (1), spin conservation and isotropy in spin space ensure that $\mathcal{S}^{\alpha\beta}(\mathbf{Q},\omega) = 0$ for $\alpha \neq \beta$, and all diagonal spin components are equivalent, $\mathcal{S}^{xx}(\mathbf{Q},\omega) = \mathcal{S}^{yy}(\mathbf{Q},\omega) = \mathcal{S}^{zz}(\mathbf{Q},\omega)$. At $T = 0$, this is given by

$$\mathcal{S}^{xx}(\mathbf{Q},\omega) = \frac{1}{2}\mathcal{S}^{+-}(\mathbf{Q},\omega) = \frac{1}{2} \sum_\lambda |\langle \Psi_\lambda(k) | S^+_{\mathbf{Q}} | \Psi_G \rangle|^2 \delta(\omega - \omega_\lambda),$$

where λ labels the eigenstates of H and

$$S^+_{\mathbf{Q}} = \frac{1}{\sqrt{2N_d}} \sum_{m=1}^{N_d} \sum_{p=\pm} \exp(i\mathbf{Q}\cdot\mathbf{r}_{m,p}) S^+_{m,p}$$

is the Fourier-transformed spin creation operator.

The action of the neutron is to flip a spin and so create a localized spin-1 polarization in the chain, and the strength of scattering to particular states is determined by their overlap with this spin-flip state. This means that the multiparticle states will be sampled with particles created close together. This is where interactions of the particle wave functions are most important, making neutrons a sensitive technique for looking at overlap effects. An interesting consequence of this is that the short-range interactions between particles can have a large influence on measured correlation functions with little effect on the thermodynamics of the spin chain, an effect noted for spinons in uniform chains.[22] Similarly, the thermodynamic influence of bound states at low temperatures vanishes as $1/N$, yet they have a finite scattering cross section as discussed below.

B. Neutron scattering measurements

We made our measurements of the inelastic scattering cross section of CN using the SPINS cold-neutron triple-axis spectrometer at the NIST Center for Neutron Research. The same high-quality sample of copper nitrate used by Xu[10] was utilized. This 14.1-g sample consists of four coaligned single crystals of CN, with deuterium substituting for 92% of hydrogen. The substitution of D for H was made as it reduces significantly the background from incoherent scattering of neutrons but does not change the magnetic properties of the material. The sample was mounted with $(h,0,l)$ as the scattering plane in a pumped ^{3}He cryostat at a base temperature of 300 mK. This temperature is an order of magnitude

smaller than the gap energy (~4.4 K), and the collective quantum ground state is almost entirely free of thermally produced magnons, with a population of these numbering less than 1 per 2×10^6 dimer sites.

The two-magnon scattering is expected to be weak as the neutron matrix element to it is of $\mathcal{O}(\alpha^2)$ from the ground state, so the spectrometer was set up in an open configuration to gain maximum scattered signal, and the only collimator included in the setup was of 80′ between monochromator and sample. A vertically focused pyrolytic graphite PG(002) array monochromated the incident neutrons (energy E_i, wave vector $\mathbf{k}_i$), and a horizontally focused array composed of eleven independently rotatable PG(002) blades was employed to analyze the scattered neutrons (E_f, $\mathbf{k}_f$). A cooled Be filter was placed in the incident beam before the sample to remove higher-order contamination from the beam. The actual neutron energy transfer to the sample being $\hbar\omega=E_i-E_f$ and the wave vector transfer is $\mathbf{Q}=\mathbf{k}_i-\mathbf{k}_f$.

Measurements of the scattering cross section were made by fixing the final energy at $E_f=2.5$ meV ($k_f=1.10$ Å^{-1}) and scanning incident energy E_i at various fixed wave number transfers along the chain, $k=\mathbf{Q}\cdot\hat{\mathbf{d}}$ (i.e., the component of the scattered wave vector along the important chain direction). Although there are actually two types of chain in CN (with repeats $\mathbf{b}=[1,1,1]/2$, and $\mathbf{b}'=[1,1,1]/2$), this is not important in our case—we study the $(h,0,l)$ scattering plane where the chains give identical contributions (see Fig. 3).

With an open scattering configuration instrumental resolution is an important consideration. The spectrometer resolution represents the spread in coordinate space $(\mathbf{Q},\omega)$ sampled by the instrument at each measured point. The energy resolution of the spectrometer is of Gaussian profile with a full width at half maximum (FWHM) at $E_f=2.5$ meV and $\hbar\omega=0.8$ meV of ~0.10 meV. The $\mathbf{Q}$ resolution is dominated by the wide angular acceptance (14°) of the analyzer on the scattered side—it is highly elongated along a direction within the scattering plane that is perpendicular to the scattered wave vector—and approximating the measured angular dependence by a Gaussian profile gives a FWHM of ~0.2 Å^{-1}. This resolution width is very considerable; however, by using calculated scan trajectories that maintain the final wave vector $\mathbf{k}_f$ along the crystallographic (1,0,1) direction, so as to integrate over the nondispersive directions between chains, good wave number resolution in k along the important quantum spin chain directions (estimated at of order 0.02 Å^{-1}) is maintained.

V. RESULTS AND ANALYSIS

Figure 4 shows some of the results of scans in energy performed on CN: Panel (a) shows a scan at the antiferromagnetic zone center, $k=2\pi/d$, taken at $T=300$ mK. This is the wave number along the chain where the magnon energy is a minimum; cf. Fig. 1. Strong elastic scattering from incoherent nuclear processes is clearly seen as well as a peak at 0.4 meV as expected for the one magnon mode,[10] close to the dimer excitation energy $J=0.45$ meV. A second much weaker peak appears at roughly double the dimer energy at about 0.9 meV, which is where two-magnon scattering is

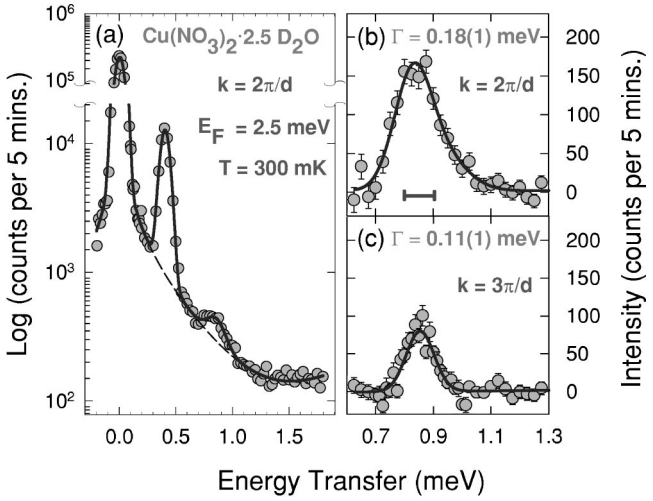

FIG. 4. (a) Low-temperature scattering at $k=2\pi/d$. The dashed line is a fitted background, and the solid line is a fit to the scattering described in the text. (b) Two-magnon scattering with background subtracted off. The solid line is a fit (see text). The solid bar indicates the instrumental resolution. (c) Two-magnon scattering for $k=3\pi/d$ with nonmagnetic background subtracted off.

expected. On heating up the sample both the 0.4 meV and 0.9 meV peaks disappear, identifying these as being magnetic in origin.

Heating up the sample also identifies the nonmagnetic background contribution (dashed line in the figure) which consists of the incoherent nuclear peak, modeled by a Gaussian centered at zero energy, and a broad contribution from thermal diffuse scattering from the analyzer which is well characterized by a power-times-Lorentzian (broad, quasielastic) component decaying from zero energy. As the background is large compared to the two-magnon signal it was studied in depth at different temperatures and wave vectors.

Panels (b) and (c) of Fig. 4 show this peak with the modeled nonmagnetic background subtracted at $k=2\pi/d$ and $k=3\pi/d$, respectively. This feature is considerably weaker than the one-magnon scattering. The FWHM of the peak narrows from 0.18(1) meV at $2\pi/d$, panel (b), to 0.11(1) meV at the zone boundary $(3\pi/d)$, panel (c), behavior indeed consistent with two-magnon scattering.

Figure 1 shows the energy corresponding to a weighted average of scattering as a thick gray line. It is notable that at $k=3\pi/d$ to a good approximation the neutrons couple only to the bound mode, so that nearly all the scattering weight is in it, not the continuum. The calculated neutron scattering intensity from the bound state is ~2% of the one-magnon intensity which agrees with the data in Fig. 4.

The one- and two-magnon scattering at 300 mK was scanned from $k=\pi/d$ to $5\pi/d$ in steps of $\pi/4d$. The background-subtracted data are plotted in the upper panel of Fig. 5. The lower panel shows the calculated magnetic scattering based on the 1D perturbation theory of the Appendix with the estimated parameters $J=0.45$ and $\alpha=0.27$. The calculation includes the correct dimer structure factor effects and uses the true scan trajectories in conjunction with the

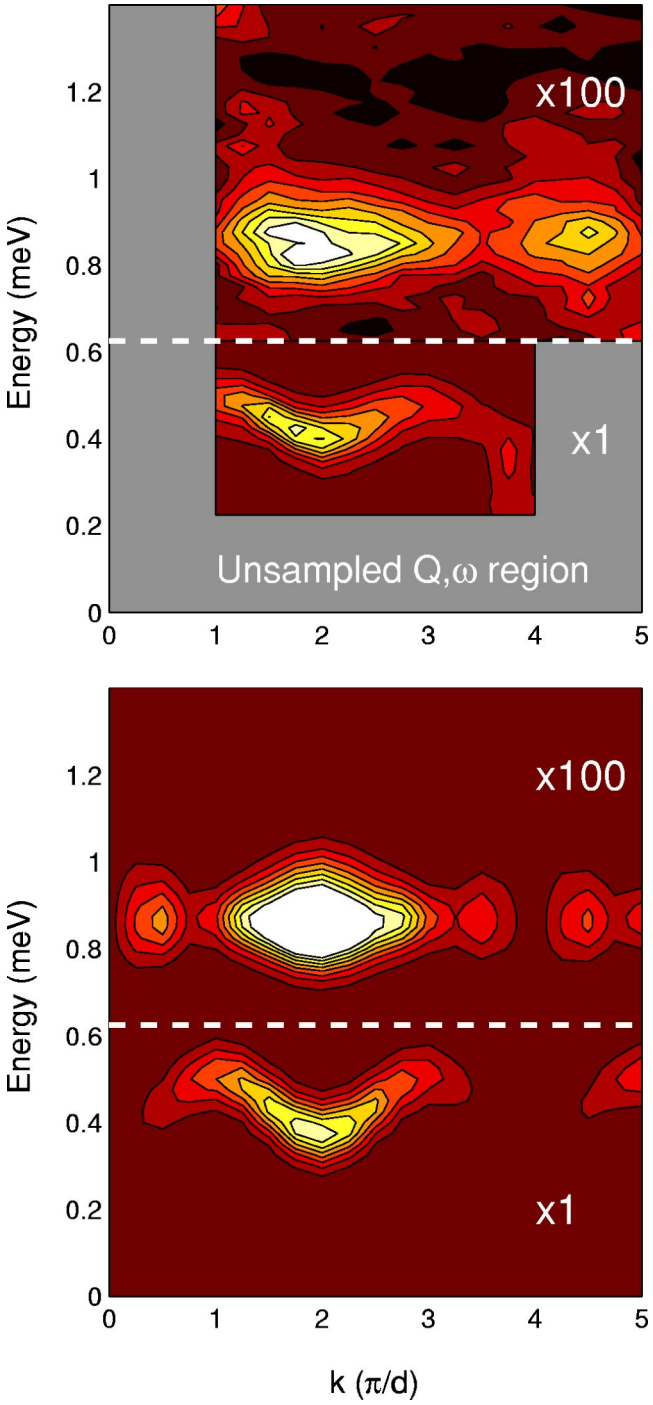

FIG. 5. (Color online) Upper panel shows a filled contour plot of the measured data with nonmagnetic background subtracted. Intensity is on a linear scale going from dark (minimum) to light (maximum). The two-magnon scattering has been enhanced by a factor of 100 to make it visible on the same scale. Lower panel shows the calculated scattering using perturbation theory with corrections for instrumental resolution, multiple scattering, and magnetic form factor.

dimer coordinates given in Table I. Corrections for the Cu^{2+} magnetic form factor[23] have also been made. Instrumental line broadening has been included as well by convolving the theoretical calculations with the estimated instrumental resolution and sample mosaic spread. The calculation is directly comparable with the data in the upper panel of Fig. 5, and at a qualitative level there is good agreement with experiment.

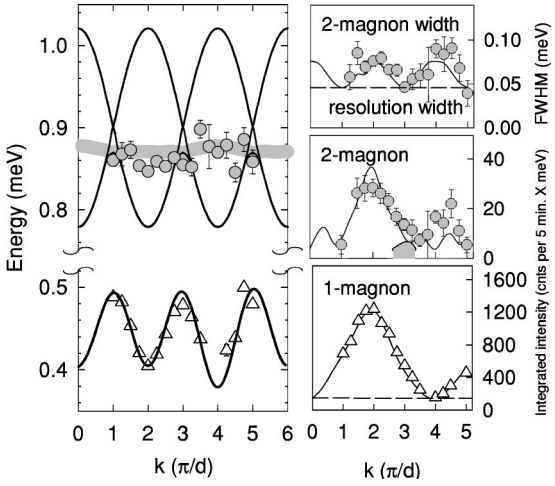

FIG. 6. Comparison of theory and data. Left panel shows fitted positions of observed scattering using perturbation theory (see text). Right lower panel shows fitted one magnon intensity compared with perturbation theory (see text). Right upper panel shows a comparison of the two-magnon width and right middle panel two-magnon intensity, with perturbation theory (see text).

Next we consider the measured one- and two-magnon scattering in more detail and relate this to the physical picture presented by perturbation theory. A quantitative comparison between theory and data is shown in Fig. 6. The measured positions of one- and two-magnon peaks are plotted in the left panel. Energies, widths, and intensities for each peak were extracted by least-squares fitting of Gaussians. In fact the wave vector and energy resolution was not sufficiently good in this experiment to distinguish details of the line shape, and the energies, widths, and intensities represent the meaningful content of the measured data. We examine the one-magnon scattering first.

A. One-magnon scattering

Dispersion The measured dispersion of the one-magnon states is shown in the left-hand panel of Fig. 6. Considerable dispersion of the one-magnon modes around the dimer energy (0.45 meV) is evident as expected. Although the one-magnon dispersion has been calculated to high order $\mathcal{O}(\alpha^5)$ (Ref. 11) previously, the small value of α in CN ensures that the one-magnon dispersion should be well approximated (to within 3%) by the $\mathcal{O}(\alpha)$ result, Eq. (2). In fact the dispersions in CN measured by Xu[10] and Stone[24] show that it is well described by

$$\omega(\mathbf{Q}) = J - \frac{1}{2}\sum_{\mathbf{u}} J_{\mathbf{u}} \cos(\mathbf{Q}\cdot\mathbf{u}), \tag{3}$$

with $J=0.442(2)$ meV the dimer coupling and $J_{[111]/2}=0.106(2)$ meV the along chain coupling, plus additional weak interdimer couplings $J'_{[1/2,0,0]}=0.012(2)$ meV and $J'_{[0,0,1/2]}=0.018(2)$ meV. The alternation ratio that Xu *et al.* consider, $\alpha = J_{[111]/2}/J = 0.240(5)$, is smaller than that found

from the magnetization data discussed above which is presumably due to the neglect of interchain coupling effects in the analysis of the latter.

The solid line through the one-magnon dispersion in Fig. 6 is that calculated using the results of Ref. 10, and it gives a reasonable account of the data. The small discrepancies from the peak centers measured here are attributable to the effects of the instrumental resolution which averages over a large swathe of the interchain dispersion modulation. Indeed the averaging procedure means that the predicted (3%) deviations of the dispersion relation away from the first-order expression, Eq. (3),[11] are not resolvable in this experiment.

Intensity The lower right-hand panel of Fig. 6 shows the one-magnon intensities extracted from fitting. The neutron scattering matrix element $\mathcal{S}^{+-}(\mathbf{Q}) \equiv |\langle \Psi_\lambda(k)|S^+_{\mathbf{Q}}|\Psi_G\rangle|^2$ for excitation of the one-magnon states in the AHC to $\mathcal{O}(\alpha^3)$ is[11]

$$\mathcal{S}^{+-}_{1\mathrm{mag}}(\mathbf{Q}) = [1-\cos(\mathbf{Q}\cdot\rho)]\left\{\left(1-\frac{5}{16}\alpha^2-\frac{3}{32}\alpha^3\right)+\left(\frac{1}{2}\alpha-\frac{1}{8}\alpha^2-\frac{5}{192}\alpha^3\right)\cos(kd)+\left(\frac{3}{16}\alpha^2+\frac{7}{48}\alpha^3\right)\cos(2kd)+\frac{5}{64}\alpha^3\cos(3kd)\right\}. \quad (4)$$

The leading-order scattering process is from the bare dimer component of the ground state, and the $\alpha/2\cos(kd)$ component in the one-magnon structure factor arises from an $\mathcal{O}(\alpha)$ two-dimer excitation in the ground state. The dynamical structure factor then reflects both the composition of the ground and excited states, leading to a complex wave vector dependence. It is worth noting that for small α the higher-order terms in Eq. (4) rapidly decrease in intensity and for CN the $\mathcal{O}(\alpha^3)$ term in Eq. (4) is already of negligible size ($<0.5\%$).

An interesting aspect of the one-magnon intensity $\mathcal{S}^{+-}_{1\mathrm{mag}}(\mathbf{Q})$ noted in Ref. 11 is that the spin structure factor comes in only as a $[1-\cos(\mathbf{Q}\cdot\boldsymbol{\rho})]$ modulation. So where $\mathbf{Q}\cdot\boldsymbol{\rho}=2\pi n$ (n integer) the magnetic intensity should be zero. Although this situation occurs for the measurements at the wave number $k=3.9\pi/d$, the scattering does not go to zero because of residual intensity due to strong incoherent scattering processes. Such residual scattering was also observed in CN by Xu.[10]

The mechanism behind this residual scattering is as follows: a neutron scatters inelastically with wave vector and energy transfer $(\mathbf{k},\omega')$; it then has a small probability for scattering elastically via an incoherent scattering process which changes its wave vector yet again before leaving the sample. This double-scattering process is proportional to the one-magnon cross section $\mathcal{S}^{1\mathrm{mag}}(\mathbf{k},\omega)$ convolved with the incoherent cross section $\mathcal{S}^{\mathrm{inc}}(\mathbf{k},\omega)$, $\mathcal{S}^{2\mathrm{nd}}(\mathbf{Q},\omega) = A\int d\mathbf{k}d\omega' \mathcal{S}^{1\mathrm{mag}}(\mathbf{k},\omega')\mathcal{S}^{\mathrm{inc}}(\mathbf{Q}-\mathbf{k},\omega-\omega')$. As the scattering from the incoherent process is elastic and independent of wave vector $[\mathcal{S}^{\mathrm{inc}}(\mathbf{k},\omega)\sim\sigma_{\mathrm{inc}}\delta(\omega)]$ the secondary scattering appears as a wave-vector-independent band $\mathcal{S}^{2\mathrm{nd}}(\mathbf{Q},\omega) = A\sigma_{\mathrm{inc}}\int d\mathbf{k}\mathcal{S}^{1\mathrm{mag}}(\mathbf{k},\omega)$ underlying the one-magnon scattering. The ready observability of this multiple-scattering effect is due to the very large incoherent cross section of hydrogen and the large sample size. The solid line in the figure then is the scattering intensity predicted using Eq. (4) with $J=0.45$ meV and $\alpha=0.27$ including a constant wave-vector-independent secondary scattering contribution (dashed line), as well as instrumental resolution and magnetic form factor. It is seen to account very well for the observed scattering intensity. We now consider the two-magnon scattering.

B. Two-magnon scattering

Integrated peak intensities, widths, and positions extracted using the fitting method described above for the two-magnon scattering are also plotted in Fig. 6. The peak positions are plotted in the left panel of Fig. 6 (solid circles). They are nearly dispersionless at an energy of $\sim$0.86 meV. The peak widths are plotted in the top right-hand panel. These are largest around $k=2\pi/d$ and $4\pi/d$ where the continuum is expected to be widest, and are near resolution limited around π/d, $3\pi/d$, and $5\pi/d$. Also shown is the integrated peak intensity $\int d\omega I(\omega)$, where $I(\omega)$ is the intensity, which peaks around $k=2\pi/d$.

Intensity The integrated peak intensity of the measured two-magnon scattering plotted in Fig. 6 is a sum over both the two-magnon continuum *and* the $S=1$ bound mode. To calculate the intensity predicted by the perturbative analysis of the AHC presented here the expressions for the two-magnon continuum and bound-state wave functions derived in the Appendix are used. For the two-magnon continuum contribution account of the density of momentum states with energy transfer is taken, and the scattering intensity is calculated numerically using Eqs. (A5) and (A14). In the range $|n\pi-kd|\leqslant\pi/3$, where n is an odd integer, the $S=1$ bound state also exists and contributes to the intensity too. This contribution is calculated directly from Eq. (A17) and added to the integrated intensity of the continuum.

As interchain effects are effectively integrated over in the two-magnon scattering, and this results in line broadening rather than shifts in energy; we thus have implicitly included interchain coupling effects in our definition of $\alpha=0.27$ for Eq. (1). The calculated integrated intensity of the continuum +bound mode is shown as the solid line in the center right-hand panel of Fig. 6. It includes corrections for instrumental resolution, magnetic form factor, and residual secondary scattering from incoherent processes (see above). The bound mode contribution by itself (with residual scattering added) is indicated by the shaded area in the panel.

It is evident from the figure that the integrated two-magnon intensity data $\int d\omega I(\omega)$ (right middle panel) show a more complicated k dependence than the one-magnon scattering. The comparison with the theoretical calculation (solid line) looks qualitatively similar to the data; however, it underestimates the scattering at $k\approx 9\pi/2d$ and overestimates it at $2\pi/d$, which may indicate that higher-order terms in the scattering amplitude than considered here are important. A

notable feature of the two-magnon intensity calculation is that its k dependence is very strongly dependent on the spatial arrangement of the magnetic ions. However, this cannot explain the observed differences from the data as the one-magnon intensity provides an independent confirmation that the spatial positions used in the calculation are correct.

Center The fitted peak centers are compared with the computed weighted center $\langle\omega\rangle = \int d\omega I(\omega) \times \omega$ (gray band) for the $\mathcal{O}(\alpha^2)$ perturbation theory in the left panel of Fig. 6. The nearly dispersionless extracted positions (gray solid circles) are located at the calculated weighted-average energies (gray band) replotted from Fig. 1. The fact that the weighted center lies below the center of the continuum is a direct result of the movement of scattering weight towards the lower boundary due to the magnon-magnon interaction.

Width The peak widths obtained from the fits are shown in the top right-hand panel. The solid line represents that calculated using the perturbation theory. It is the sum in quadrature of the instrumental resolution width in energy and the variance σ of the theoretical intensity where $\sigma^2 = \int d\omega I(\omega) \times (\omega - \langle\omega\rangle)^2$. The calculation is seen to provide a good account of the data.

Bound mode Undoubtedly one of the most interesting aspects of the multiparticle states in the AHC is the proposed existence of the bound mode below the two-magnon continuum. The perturbation theory presented in the Appendix gives the functional form for the wave vector dependence of the bound mode's neutron scattering cross section,

$$\mathcal{S}^{+-}_{\mathrm{BS}}(\mathbf{Q}) = \left(\frac{\alpha}{4}\right)^2 [1 - 4\cos^2(kd/2)] \times \{\sin[\mathbf{Q}\cdot(\rho+\mathbf{d})/2] + 3\sin[\mathbf{Q}\cdot(\rho-\mathbf{d})/2]\}^2,$$

and for the wave vectors $\mathbf{Q}$ probed in this experiment the bound mode is predicted to be most prominent in the narrow region around $k = 3\pi/d$ with an extent and strength as indicated by the shaded contribution in the middle right panel of Fig. 6. In fact at the $k = 3\pi/d$ point itself the scattering intensity of the two-magnon continuum is predicted to vanish and the measured intensity at this point [see Fig. 4(c)] should be from just the bound mode with a small background from the residual secondary scattering.

At the $k = 3\pi/d$ point [Fig. 4(c)] a sharp, resolution-limited mode is indeed seen, consistent with scattering to the $S = 1$ bound mode. However, if for some reason an additional unidentified effect were present which nullified the binding mechanism and that also gave an enhanced scattering to the continuum at this point, then quite sharp scattering would also occur, this time due to the fact that the continuum is narrow in energy around $k = 3\pi/d$. In this regard it is worthwhile considering the peak position in energy as any bound mode must be at a lower energy than the continuum lower boundary (which is a sum of one-magnon energies).

Fitting the scattering in CN at the $k = 3\pi/d$ point [Fig. 4(c)] gives a peak centered at 0.852 ± 0.007 meV. This gives a positive binding energy (the energy difference by which the peak is lower than the calculated two-magnon continuum) of $E_B = 0.03 \pm 0.02$ meV (note that the large error bar here takes into account the interchain coupling and uncertaintly in coupling constants used to calculate the continuum lower boundary—high-order results from Ref. 11 have been used here for accuracy). In fact the binding energy of the $S = 1$ state for an idealized AHC is predicted to be[11] $E_B = J(\frac{1}{4}\alpha - \frac{13}{32}\alpha^2) = 0.017$ meV for CN, which is consistent with our measurements. However, although the energy, sharpness, and observed intensity of the scattering around $k = 3\pi/d$ lends support to binding around this bandwidth minimum, the experimental error in the binding energy is too large for it to constitute definitive proof of the effect in CN, and further experiments are needed that would resolve the bound mode form the continuum.

VI. DISCUSSION

Our measurements establish the feasibility of studying weak multimagnon states using neutron scattering and raise a number of important issues. First, the introduction of experimental data highlights the need for practical techniques for calculating the multiparticle excitation spectra and cross sections for realistic spin models. Our perturbation theory, although useful for interpreting results, is of too low order to quantitatively account for our measurements and in addition does not include interchain coupling. Very powerful linked-cluster-expansion techniques have recently been introduced that allow multiparticle spectra to be calculated to high order[25,26] for the AHC, and the extension of these to calculations of the neutron scattering cross section would be a significant development. Analytical approaches based on Green function techniques may also prove fruitful. Second, measurement of weak multiparticle signals preludes the access of neutron scattering to measuring bound two-magnon states. Interactions such as next-nearest-neighbor coupling should further stabilize bound modes and make measurement of these easier. A question which requires further investigation is the stability of such bound modes to thermal fluctuations and also interchain coupling. An alternative route for investigating the phenomenology of particle binding is through solitonic systems such as the 1D Ising chain with small XY-like terms.[27] In this case the coupling of neutrons to pairs of $S = 1/2$ solitons (also called spinons) is at zeroth order and therefore strong. Binding of solitons only occurs when extra terms are included in the Hamiltonian, such as exchange mixing,[28] next-nearest-neighbor coupling,[29] or transverse field.[30] Evidence for this binding phenomenon and Ising-like chains has been observed recently in neutron scattering experiments.[28]

Time-of-flight (TOF) neutron spectrometers give potentially much better energy resolution than conventional triple-axis instrumentation and could provide definitive proof of the bound state in the alternating chain by resolving the bound mode from the continuum. Previously, TOF techniques have proved successful in the study of similar binding effects at the bandwidth minimum of the two-soliton continuum scattering of the $S = 1/2$ XXZ Ising chain material $CsCoCl_3$.[28] Although limited neutron fluxes may make such measurements difficult for CN,[10] these should be feasible and we plan to make such measurements in the near future.

TABLE II. Eigenstates of dimer m, $H_m = J\mathbf{S}_{m,-}\cdot\mathbf{S}_{m,+}$.

Label	Ψ_m	E	S_m^z	S_m
G_m	$\frac{1}{\sqrt{2}}\{\lvert\uparrow\downarrow\rangle - \lvert\downarrow\uparrow\rangle\}$	$-3J/4$	0	0
1_m	$\lvert\uparrow\uparrow\rangle$	$J/4$	1	1
0_m	$\frac{1}{\sqrt{2}}\{\lvert\uparrow\downarrow\rangle + \lvert\downarrow\uparrow\rangle\}$	$J/4$	0	1
$\overline{1}_m$	$\lvert\downarrow\downarrow\rangle$	$J/4$	-1	1

VII. SUMMARY

In summary, we have used inelastic neutron scattering to investigate the ground and excited states of the near-ideal alternating Heisenberg chain material $Cu(NO_3)_2\cdot 2.5D_2O$, and also derived the scattering analytically to lowest order in perturbation theory. Our measurements are consistent with the predictions of this model for several magnetic properties of this system, including the ground-state energy, one- and two-magnon excitation spectra and intensities, and possibly the existence of a two-magnon bound state. Much experimental work remains to be done to establish the phenomenology of binding in isotropic 1D systems.

ACKNOWLEDGMENTS

We wish to thank Dr. B. Lebech, Dr. R. Hazell, Dr. B. Lake, Dr. P-A Lindgård, and Dr. D. McMorrow for their help and advice and also Risø National Laboratory for generous support. This work was partly supported by Oak Ridge National Laboratory, managed by UT-Battelle, LLC, for the U.S. Department of Energy under Contract No. DE-AC05-00OR22725. The NSF supported work at SPINS through Grant No. DMR-9423101 and work at JHU through Grant Nos. DMR-9453362 and DMR-9801742. D.H.R. acknowledges the generous support of the David and Lucile Packard Foundation. Work at Harvard (K.D.) was supported by NSF-DMR Grant Nos. 9981283, 9714725, and 9976621

APPENDIX

1. Ground state

Here we apply the perturbation theory of Ref. 11 to two-magnon scattering. The single dimer eigenstates (labeled G,1,0,1) are listed in Table II, and the ground state of the uncoupled dimers ($\alpha=0$) is a direct product of dimer ground states:

$$\Psi_0 = \prod_{m=1}^{N_d} \lvert G_m\rangle,\quad E_0 = -\frac{3JN_d}{4}. \tag{A1}$$

As total spin $S_T = \Sigma_{m=1}^{N_d} S_m$ and $S_T^z = \Sigma_{m=1}^{N_d} S_m^z$ are constants of the motion for the Hamiltonian H they organize the Hilbert space. For notation we introduce dimer creation operators $a_m^+\lvert G_m\rangle = \lvert a_m\rangle$ where $a = 1,0,\overline{1}$ label excited dimer states. In real space we denote the singly excited states with quantum numbers $(S_T, S_T^z) = (1,a)$ as $\lvert a\rangle_m = a_m^+\Psi_0$ and the doubly excited with $\lvert (S_T, S_T^z)\rangle_{m,\nu}$ as the Clebsh-Gordan combinations of excitations at dimer sites m and $m+\nu$, i.e., $\lvert(0,0)\rangle_{m,\nu} = 1/\sqrt{3}\{1_m^+\overline{1}_{m+\nu}^+ - 0_m^+0_{m+\nu}^+ + \overline{1}_m^+1_{m+\nu}^+\}\Psi_0$, $\lvert(1,1)\rangle_{m,\nu} = 1/\sqrt{2}\{0_m^+1_{m+\nu}^+ - 1_m^+0_{m+\nu}^+\}\Psi_0$, etc.

As the alternating chain has translational symmetry plane-wave states prove convenient,

$$\lvert a\rangle_k \equiv \frac{1}{\sqrt{N_d}}\sum_{m=1}^{N_d} e^{imkd}\lvert a\rangle_m \tag{A2}$$

and

$$\lvert (S,S^z)\rangle_{k,\nu} \equiv \frac{1}{\sqrt{N_d}}\sum_{m=1}^{N_d} e^{imkd}\lvert (S,S^z)\rangle_{m,\nu}, \tag{A3}$$

where the allowed momenta are $k_n = 2n\pi/N_d d$, where n are integers from $-N_d/2$ to $N_d/2$. The action of the Hamiltonian on the basis states has been considered in Ref. 11, and the ground state to $\mathcal{O}(\alpha)$ is

$$\Psi_G = \eta_0\left[\Psi_0 - \alpha\frac{\sqrt{3}}{8}\sum_{m=1}^{N_d}\lvert(0,0)\rangle_{m,1}\right], \tag{A4}$$

where $\eta_0 = 1-(3/128)\alpha^2 N_d$.

Neutron scattering measures the square of the expectation value of the spin operator $S^+(\mathbf{Q}) = (2N_d)^{-1/2}\Sigma_{m=1}^{N_d}\Sigma_{p=\pm}\exp(i\mathbf{Q}\cdot\mathbf{r}_{m,p})S_{m,p}^+$ between eigenstates, where $\mathbf{Q}$ is the wave vector transfer of the neutron. The action of this spin operator applied to the ground state is

$$S^+(\mathbf{Q})\lvert\Psi_G\rangle = A_{\mathbf{Q}}\lvert 1\rangle_k + B_{\mathbf{Q}}\lvert(1,1)\rangle_{k,1},$$

$$A_{\mathbf{Q}} = \frac{1}{\sqrt{2}}(e^{i\mathbf{Q}\cdot\rho/2} - e^{-i\mathbf{Q}\cdot\rho/2})\left(1+\frac{\alpha}{4}\cos(kd)\right),$$

$$B_{\mathbf{Q}} = \frac{\alpha}{8}(e^{i\mathbf{Q}\cdot\rho/2} + e^{-i\mathbf{Q}\cdot\rho/2})(e^{ikd}-1), \tag{A5}$$

where $k = \mathbf{Q}\cdot\hat{\mathbf{d}}$ is the wave number of the states excited by this operator. The neutron scattering matrix element at $T=0$ to state λ is given by $\mathcal{S}_\lambda^{+-}(\mathbf{Q}) = \lvert\langle\Psi_\lambda\rvert S_{\mathbf{Q}}^+\lvert\Psi_G\rangle\rvert^2$.

2. One-magnon states

The one-magnon wave functions to order $\mathcal{O}(\alpha)$ are[11]

$$\Psi_{1\mathrm{mag}} = \lvert a\rangle_k + \frac{\alpha}{2\sqrt{2}}(e^{ikd}+1)\lvert(1,a)\rangle_{k,1} - \frac{\alpha\sqrt{3}}{8\sqrt{N_d}}\sum_{m,m'=1}^{N_d}\delta_{m\neq m'}e^{imkd}a_m^+\lvert(0,0)\rangle_{m',1} \tag{A6}$$

and form an $S=1$ triplet with an energy gap $\Delta = J-\alpha J/2$ above the ground state and dispersion:

$$\omega_{1\mathrm{mag}}(k) = J - \alpha J/2 \cos(kd). \tag{A7}$$

Application of the $S^+(\mathbf{Q})$ operator gives the intensity to $\mathcal{O}(\alpha)$:

$$\mathcal{S}^{+-}_{1\mathrm{mag}}(\mathbf{Q}) = [1-\cos(\mathbf{Q}\cdot\rho)]\left\{1+\frac{1}{2}\alpha\cos(kd)\right\}.$$

3. Two-magnon states

Ignoring states higher than two-excited-dimer (as they do not contribute to the neutron scattering matrix element to lowest order in α), the action of the Hamiltonian is[11]

$$H|a\rangle_k = \alpha_k|a\rangle_k + \sqrt{2}\,\gamma_k^\dagger|(1,a)\rangle_{k,1}$$

and

$$H|(1,a)\rangle_{k,\nu} = \begin{cases} \sqrt{2}\,\gamma_k|a\rangle_k + (\beta-\epsilon)|(1,a)\rangle_{k,1} + \gamma_k|(1,a)\rangle_{k,2}, & \nu=1, \\ \beta|(1,a)\rangle_{k,\nu} + \gamma_k|(1,a)\rangle_{k,\nu+1} + \gamma_k^\dagger|(1,a)\rangle_{k,\nu-1}, & \nu>1, \end{cases} \tag{A8}$$

where $\alpha_k = J-(\alpha J/2)\cos(kd)$, $\beta = 2J$, $\epsilon = \alpha J/4$, $\gamma_k = -(\alpha J/4)(1+e^{-ikd})$, and $\dagger$ denotes complex conjugation. The excitation spectrum can be calculated by direct diagonalization of a large number of dimers and application of the matrix element above or by analytical solution.

Approximate analytical wave functions for the $S=1$ states can be calculated using elementary scattering theory; see Ref. 29. Ignoring the coupling to the one-excited-dimer states for the time being, the two-magnon wave functions are

$$\Psi_{2\mathrm{mag}}(k) = \sum_{\nu=1}^{N_d-1} b_\nu \exp(i\theta\nu)|(1,1)\rangle_{k,\nu}. \tag{A9}$$

where for $\theta = -i\ln(\sqrt{\gamma_k^\dagger/\gamma_k}) = kd/2$ the time-independent Schrödinger equation reduces to solving the real and symmetric system of equations,

$$\lambda b_1 = (\beta-\epsilon)b_1 + \tilde{\gamma}_k b_2,$$

$$\vdots$$

$$\lambda b_\nu = \beta b_\nu + \tilde{\gamma}_k(b_{\nu+1}+b_{\nu-1}),$$

$$\vdots$$

$$\lambda b_{N_d-1} = (\beta-\epsilon)b_{N_d-1} + \tilde{\gamma}_k b_{N_d-2}, \tag{A10}$$

where $\tilde{\gamma}_k = \sqrt{\gamma_k^\dagger\gamma_k} = \alpha J|\cos(kd/2)|/2$ and the term $\exp(i\theta\nu)$ serves to transform to the center-of-momentum (center R) frame where magnons are at $r_i = R-\nu/2$ and $r_j = R+\nu/2$ with total momentum $K = k_1+k_2 = kd$.

a. Magnon-pair-state solutions

Magnon pair states comprise particles that are free at large distances, and for particle conservation in one dimension the interactions introduce a phase factor ϕ on scattering. This state corresponds to

$$b_\nu^\mu = X_0\{\exp(ip_\mu\nu) - \exp[-i(p_\mu\nu-\phi_\mu)]\}, \tag{A11}$$

where the normalization constant $X_0 \simeq 1/\sqrt{N_d}$, p_μ is the relative momentum, and $\mu = 1,2,\ldots,N_d-1$ index the eigenstates. The phases and momenta are determined by the boundary conditions of the particles and their interaction energy. The standard method of solving for these boundary conditions[29,31] is to introduce the single-site coefficients b_0 and b_N and set $\epsilon b_1 = \tilde{\gamma}_k b_0$ and $\epsilon b_{N_d-1} = \tilde{\gamma}_k b_{N_d}$ and substitute into Eq. (A10). The momentum p_μ and phase ϕ_μ solve for the constraints on b_0 and b_{N_d} when

$$e^{i\phi_\mu} = \frac{\tilde{\gamma}_k + \epsilon\exp\left(-i\dfrac{\pi\mu+\phi_\mu}{N_d}\right)}{\tilde{\gamma}_k + \epsilon\exp\left(i\dfrac{\pi\mu+\phi_\mu}{N_d}\right)}, \quad p_\mu = \frac{\pi\mu+\phi_\mu}{N_d}, \tag{A12}$$

and the eigenvalues are $\lambda_\mu = 2J - \alpha J\cos(kd)\cos(p_\mu) + \mathcal{O}(1/N_d)$. In the time-dependent Schrödinger picture this state corresponds to two particles with wave packets at positions $r_i = R+\nu/2$ and $r_j = R-\nu/2$ and with momenta $k_1 = (K+p)/2$ and $k_2 = (K-p)/2$ that scatter via the **S** matrix $\mathbf{S}_{k_1,k_2} = -\exp(i\phi_{k_1-k_2})$, and the eigenspectrum is

$$\omega_{k_1,k_2} = \omega_{1\mathrm{mag}}(k_1) + \omega_{1\mathrm{mag}}(k_2), \tag{A13}$$

with $\omega_{1\mathrm{mag}}(k) = J - \alpha J\cos(kd)/2$ as above.

Including the coupling to the $|1\rangle_k$ states as a perturbation gives the approximate wave function

$$\Psi_{2\mathrm{mag}}(k,\mu) = -\frac{\alpha c_1^\mu}{2\sqrt{2}}(1+e^{-ikd})|1\rangle_k + \sum_{\nu=1}^{N_d-1} c_\nu^\mu|(1,1)\rangle_{k,\nu}, \tag{A14}$$

where $c_\nu^\mu = b_\nu^\mu\exp(ikd\nu/2)$. The neutron scattering matrix element can then be computed straightforwardly for a large-N_d system by evaluating the closure with Eq. (A5).

b. Bound-state solutions

When $\tilde{\gamma}_k < \epsilon$, ϕ_μ cannot be solved with $\mu=1$ and N_d-1, and the c_ν^1 and $c_\nu^{N_d-1}$ solutions comprise exponentially decaying bound-state solutions below the two-magnon continuum. The $S=1$ bound-state wave functions and energy have previously been given by Ühring and Schulz[9] and Damle and Nagler.[13] It is specified by Eq. (A14) with

$$b_\nu^1 = \sqrt{\frac{\epsilon^2-\tilde{\gamma}_k^2}{\tilde{\gamma}_k^2}}\exp(-\kappa\nu), \tag{A15}$$

where $\exp(-\kappa) = -\tilde{\gamma}_k/\epsilon$ which has dispersion energy

$$\omega_{\mathrm{BS}} = 2J - \frac{\alpha J}{4}[4\cos^2(kd/2) + 1]. \tag{A16}$$

An interesting feature of the bound-state solution is that it only exists over the range $|n\pi - kd| \leqslant \pi/3$, where n is an odd integer, and so there is an $S=1$ bound mode only for small wave vectors around the narrowest part of the continuum. Using our wave function we calculate the neutron scattering strength from the bound state to be

$$\mathcal{S}^{+-}_{\mathrm{BS}}(\mathbf{Q}) = \left(\frac{\alpha}{4}\right)^2 [1 - 4\cos^2(kd/2)]\{\sin[\mathbf{Q}\cdot(\rho + \mathbf{d})/2] + 3\sin[\mathbf{Q}\cdot(\rho - \mathbf{d})/2]\}^2. \tag{A17}$$

[1] A. Oosawa *et al.* Physica B **294-295**, 34 (2001).
[2] T. Nikuni *et al.* Phys. Rev. Lett. **84**, 5868 (2000).
[3] B.C. Watson *et al.* Phys. Rev. Lett. **86**, 5168 (2001).
[4] W. Yu and S. Haas, Phys. Rev. B **62**, 344 (2000).
[5] T. Giamarchi and A.M. Tsvelik, Phys. Rev. B **59**, 11 398 (1999).
[6] I. Affleck, Phys. Rev. B **43**, 3215 (1991); E.S. Sorensen and I. Affleck, Phys. Rev. Lett. **71**, 1633 (1993).
[7] R. Coldea, D.A. Tennant, K. Habicht, P. Smeibidl, C. Wolters, and Z. Tylczynski, Phys. Rev. Lett. **88**, 137203 (2002).
[8] T. Barnes, Phys. Rev. B **67**, 024412 (2003).
[9] G.S. Uhrig and H.J. Schulz, Phys. Rev. B **54**, R9624 (1996).
[10] G. Xu, C. Broholm, D.H. Reich, and M.A. Adams, Phys. Rev. Lett. **84**, 4465 (2000).
[11] T. Barnes, J. Riera, and D.A. Tennant, Phys. Rev. B **59**, 11 384 (1999).
[12] R.R.P. Singh and Z. Weihong, Phys. Rev. B **59**, 9911 (1999).
[13] K. Damle and S. Sachdev, Phys. Rev. B **57**, 8307 (1998); K. Damle and S.E. Nagler, cond-mat/9904438 (unpublished).
[14] J. Garaj, Acta Chem. Scand. **22**, 1710 (1968).
[15] B. Morosin, Acta Crystallogr., Sect. B: Struct. Crystallogr. Cryst. Chem. **26**, 1203 (1970).
[16] Note that the space group for $Cu(NO_3)_2 \cdot 2.5H_2O$ has been incorrectly given in previous work as *I* 1 2/*a* 1.
[17] K.M. Diederix, J.P. Groen, J.S.J.M. Henkens, T.O. Klaassen, and N.J. Poulis, Physica B **93**, 99 (1978).
[18] J. Eckert *et al.* Phys. Rev. B **20**, 4596 (1979).
[19] K.M. Diederix *et al.* Phys. Rev. B **19**, 420 (1979).
[20] J.C. Bonner *et al.* Phys. Rev. B **27**, 248 (1983).
[21] W. Marshall and S.W. Lovesey, *Thermal Neutron Scattering* (Clarendon, Oxford, 1971).
[22] B.A. Bernevig, D. Giuliano, and R.B. Laughlin, Phys. Rev. Lett. **86**, 3392 (2002).
[23] P.J. Brown, in *International Tables for Crystallography*, edited by A.J.C. Wilson and E. Prince (Kluwer Academic, Boston, 1999), Vol. C.
[24] M. Stone *et al.* (unpublished).
[25] S. Trebst, H. Monien, C.J. Hamer, W.H. Zheng, and R.R.P. Singh, Phys. Rev. Lett. **85**, 4373 (2000).
[26] W.H. Zheng, C.J. Hamer, R.R.P. Singh, S. Trebst, and H. Monien, Phys. Rev. B **63**, 144410 (2001).
[27] N. Ishimura and H. Shiba, Prog. Theor. Phys. **63**, 743 (1980).
[28] J.P. Goff, D.A. Tennant, and S.E. Nagler, Phys. Rev. B **52**, 15 992 (1995).
[29] F. Matsubara and S. Inawashiro, Phys. Rev. B **43**, 796 (1991).
[30] A. Ghosh, J. Phys.: Condens. Matter **13**, 5205 (2001).
[31] D.C. Mattis, *The Theory of Magnetism I* (Springer-Verlag, Berlin, 1988), Chap. 5.